

INTERFEROMETRIC PROPERTIES AND PROCESSING FOR SPACEBORNE SPOTLIGHT SAR

X. Z. Ren*, Y. Qin, and L. H. Qiao

College of Information Science and Engineering, Henan University of Technology, Zhengzhou, China

Abstract—Spotlight SAR interferometry is an attractive option for high resolution mapping and monitoring. In this paper, the signal spectral characteristics and the interferometric properties of spaceborne spotlight SAR are analyzed completely, and the effect of the azimuth-variant Doppler to spotlight SAR interferometry is studied. Moreover, a new coregistration algorithm, which contains coarse coregistration, azimuth spectral filter, and accurate coregistration with adaptive subspace projection, is proposed for spotlight SAR interferometry. The algorithm is validated with real data experiment.

1. INTRODUCTION

Spotlight SAR and interferometric SAR (InSAR) are both advanced operation modes of synthetic aperture radar (SAR) [1]. Spotlight SAR offers the possibility of a very high geometric resolution in the azimuth direction by sweeping the azimuth beam from forward to backward during imaging [2–4]. On the other hand, interferometric SAR is a powerful technique used to obtain Digital Elevation Models (DEM) in remote sensing applications [5–9]. Consequently, interferometric processing of spotlight SAR data may possess high resolution mapping and monitoring capabilities.

After the launch of the German satellite TerraSAR-X in 2007, a number of high resolution spotlight SAR data suitable for interferometry became available and the first TerraSAR-X spotlight interferograms were acquired in [6]. According to [6], the key processing steps in spotlight SAR interferometry are described briefly. In [10], some necessary modifications on the InSAR algorithms to

Received 6 September 2011, Accepted 7 November 2011, Scheduled 14 November 2011

* Corresponding author: Xiao Zhen Ren ((rxz235@163.com)).

process the TerraSAR-X spotlight data are presented. Persistent scatterer interferometry is also introduced to process the TerraSAR-X high resolution spotlight data in [11, 12]. Moreover, the atmospheric phase screen for spotlight data interferometry is investigated in [13], and a spatial variation of coherence on the microrelief scale is analyzed for high resolution spotlight images in [14]. However, the analytic expressions of the azimuth spectral properties and the interferometric properties for the spotlight SAR signal are not given. Moreover, the persistent scatterer interferometry technique used may require several SAR images to detect the solitary points.

The main topics of this paper are to analysis the signal spectral characteristics and the interferometric properties of spotlight SAR. Meanwhile, a coregistration algorithm is proposed for spotlight SAR interferometry. Because X-band signals are reflected even by leaves, and small changes of the scene may cause severe decorrelation of X-band interferograms. Therefore, conventional coregistration methods can not acquire expected results, and a new coregistration algorithm, which contains coarse coregistration, azimuth spectral filter, and accurate coregistration with adaptive subspace projection, is proposed for spotlight SAR interferometry.

The paper is organized as follows. Section 2 presents the principle and signal properties of spotlight SAR. In Section 3, the interferometric requirements and the spectrum of spotlight SAR interferograms are analyzed in detail. Section 4 discusses important processing steps for spotlight SAR interferometry. The performance is investigated by real data in Section 5. Finally, Section 6 gives a brief conclusion.

2. SPOTLIGHT SAR

2.1. Principle of Spotlight SAR

The geometry of spotlight SAR is shown in Figure 1. The sensor rotates the antenna throughout the acquisition from forward to backward. Let us assume the antenna rotation at a positive rate k_ψ , so its beam center points in the direction

$$\psi_{dc}(\tau) = k_\psi \tau \quad (1)$$

where τ is the azimuth time. Because of the rotation of the antenna, the azimuth antenna pattern of spotlight SAR can be described as

$$\begin{aligned} G_{ar}(\psi(\tau)) &\simeq G_0 \operatorname{sinc}^2 \left[\frac{L}{\lambda} \left(\frac{v_s \tau}{R_0} - k_\psi \tau \right) \right] \\ &= G_0 \operatorname{sinc}^2 \left[\frac{L}{\lambda} \frac{v_s \tau}{R_0} \left(1 - \frac{R_0 k_\psi}{v_s} \right) \right] \end{aligned} \quad (2)$$

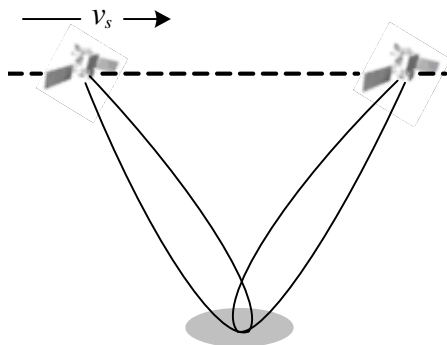


Figure 1. The geometry of spotlight SAR.

where L is the azimuth antenna size, while λ is the wavelength, v_s is the sensor velocity, and R_0 is the closest distance between the sensor and the target. From (2), we can see that the spotlight SAR can be dealt as a strip-map SAR with a fixed antenna size $L_c = \alpha L$, where α is the shrinking factor and can be described as

$$\alpha = 1 - \frac{R_0 k_\psi}{v_s} < 1 \tag{3}$$

Therefore the azimuth resolution of spotlight SAR can be approximately written as $\rho \sim \alpha L/2$. That is, the spotlight SAR can obtain better azimuth resolution than strip-map SAR.

2.2. The Signal and Spectral Properties of Spotlight SAR Data

Since the spotlight SAR data differ from the strip-map SAR data only in the azimuth direction, we can simplify the equations and consider the azimuth direction of the spotlight SAR signal only. The effective spotlight SAR azimuth raw signal of a point scatterer located at $\tau = \tau_0$ can be described as [2]

$$h_{\text{raw}}(\tau; \tau_0) = \text{rect} \left[\frac{\tau - \tau_{c0}}{T} \right] \exp [j\pi \text{FM}(\tau - \tau_0)^2] \tag{4}$$

where τ_{c0} is the center of the synthetic aperture time of the point scatterer, T is the synthetic aperture time, and FM is the frequency modulation rate

$$\text{FM} = -\frac{2v_s^2}{\lambda R_0} \tag{5}$$

Transform the signal expressed in (4) into the Doppler frequency domain, then the signal becomes

$$H_{\text{raw}}(f; \tau_0) = \text{rect}\left[\frac{f + \text{FM}\tau_0 - \text{FM}\tau_{c0}}{W_{\text{SL}}}\right] \exp\left(-j\pi\frac{f^2}{\text{FM}}\right) \exp(-j2\pi\tau_0 f) \quad (6)$$

where f is the Doppler frequency, and $W_{\text{SL}} = |\text{FM}|T$ is the azimuth bandwidth.

After the focusing of the azimuth signal, the point response of spotlight SAR will be

$$h_{\text{SL}}(\tau; \tau_0) = \text{sinc}[W_{\text{SL}}(\tau - \tau_0)] \exp[j2\pi\text{FM}(\tau_{c0} - \tau_0)(\tau - \tau_0)] \quad (7)$$

From (7) we get that the spectrum of the point scatterer located at $\tau = \tau_0$ is approximately a rectangular-shaped band-pass spectrum, at center frequency

$$f_0 = \text{FM}(\tau_{c0} - \tau_0) \quad (8)$$

For staring-spotlight mode, the antenna beam center points at the observation scene center all the time; thus the azimuth synthetic aperture time for all the scatterers are the same. That is to say, τ_{c0} is a constant. From (8), we can get that the Doppler centroid frequency varies near linearly with azimuth in staring-spotlight mode.

For sliding-spotlight mode, the synthetic aperture time of each point scatterer is shorter than the recorder raw data time; thus the point scatterers located at different azimuth positions have different synthetic aperture time centers. That is to say, τ_{c0} varies with azimuth. Since the spotlight mode provided by TerraSAR-X is sliding-spotlight mode, we focus on this mode in detail. In order to give a clear expression of the azimuth spectrum of sliding-spotlight mode, we can rewrite (8) as [3]

$$f_0 = \text{FM}(\tau_{c0} - \tau_0) = k_a\tau_0 \quad (9)$$

where k_a is the Doppler centroid rate of the focused image. From (9) we get that the Doppler centroid frequency also varies near linearly with azimuth in sliding-spotlight mode. Consequently, the point response of sliding-spotlight-mode SAR can also be described as

$$h_{\text{SL}}(\tau; \tau_0) = \text{sinc}[W_{\text{SL}}(\tau - \tau_0)] \exp[j2\pi k_a\tau_0(\tau - \tau_0)] \quad (10)$$

3. INTERFEROMETRIC PROPERTIES OF SPACEBORNE SPOTLIGHT SAR

3.1. Interferometric Requirement for Orbit Property

If the two SAR images have been acquired at different times, the structure of the scatterers may have changed in the meantime. For

example, Forests tend to decorrelate due to movement of leaves and branches. Therefore, short orbit repeat cycle may reduce the effect of the temporal decorrelation. The 11 days repeat cycle of TerraSAR-X may compensate some of the expected temporal decorrelation in X-band when compared to ERS or ENVISAT (35 days repeat). Moreover, shorter baseline can be obtained by better orbit maintenance, which can reduce the effect of the baseline decorrelation. The baseline coherence can be given by [15]

$$\gamma_{\text{baseline}} = 1 - \frac{2\rho_y \cos \theta B_{\perp}}{\lambda R_0} \quad (11)$$

where ρ_y is the range resolution, θ is the look angle, and B_{\perp} is the baseline. For the TerraSAR-X system, the expected baseline is within 350 m (standard deviation), which leads to 95% baseline coherence with the typical parameters of TerraSAR-X spotlight products [16].

3.2. Interferometric Requirement for Azimuth Scanning Pattern Synchronization

The beam center direction of spotlight SAR changes throughout the imaging acquisition, which causes a Doppler centroid frequency drift in the azimuth direction

$$f_{dc} = -\frac{2v_s}{\lambda} \sin[\psi_{dc}(\tau)] \quad (12)$$

And the Doppler centroid rate is

$$k_r = \frac{\partial f_{dc}}{\partial \tau} \simeq -\frac{2v_s}{\lambda} k_{\psi} \quad (13)$$

From (13) we get that the Doppler centroid frequency in the focused image of spotlight SAR varies near linearly with azimuth, which is different from strip-map SAR. Therefore, the variation of the processed azimuth spectrum of a spotlight SAR product should be considered in spotlight SAR interferometric processing.

Moreover, in order to form a coherent spotlight interferogram, the received Doppler frequency spectrum must overlap. That is to say, the performances achievable by an interferometric spotlight SAR system depend upon the capability to observe the same target by the same squint angle. Any mismatch $\Delta\psi$ would introduce a shift in the azimuth spectrum

$$\Delta f_{dc} \simeq \frac{2v_s}{\lambda} \Delta\psi \quad (14)$$

Because the antenna pointing error would lead to an azimuth asynchronous scanning decorrelation, and to a loss in the interferogram azimuth resolution, both images should choose the same azimuth spectrum to ensure the quality of the interferogram.

3.3. Spectrum of Spotlight SAR Interferograms

We assume the distributed scatterers input to the interferometry system with the following complex reflectivity functions [17]

$$x_1(\tau) = \sqrt{1 - \gamma_T}a(\tau) + \sqrt{\gamma_T}c(\tau) \quad (15)$$

$$x_2(\tau) = \left(\sqrt{1 - \gamma_T}b(\tau) + \sqrt{\gamma_T}c(\tau) \right) \exp(j2\pi f_\varphi \tau) \quad (16)$$

The functions $a(\tau)$, $b(\tau)$, and $c(\tau)$ are independent zero-mean white circular complex Gaussian processes. γ_T denotes the temporal coherence, and f_φ denotes an azimuth fringe frequency.

The focused spotlight SAR data is obtained by convolution with the point response function from (10) by the following integral

$$s_i(\tau) = \int h_{\text{SL}}(\tau, \tau_0)x_i(\tau_0)d\tau_0, \quad i = 1, 2 \quad (17)$$

And the autocorrelation function of the focused spotlight SAR image is given by

$$R_{ss}(t, \tau) = E \{s^*(\tau)s(\tau + t)\} \quad (18)$$

The spotlight SAR interferogram is

$$i(\tau) = s_1(\tau)s_2^*(\tau) \quad (19)$$

And the autocorrelation function of the spotlight SAR interferogram is obtained by

$$R_{ii}(t, \tau) = E \{i^*(\tau)i(\tau + t)\} = E \{s_1^*(\tau)s_2(\tau)s_1(\tau + t)s_2^*(\tau + t)\} \quad (20)$$

Submitting (10), (15), (16) and (17) into (20) yields

$$\begin{aligned} R_{ii}(t) &= W_{\text{SL}}^2 \text{tri}^2 \left(\frac{k_a t}{W_{\text{SL}}} \right) \text{sinc}^2 [(W_{\text{SL}} - |k_a t|) t] \\ &\quad + W_{\text{SL}}^2 \gamma_T^2 \text{tri}^2 \left(\frac{f_\varphi}{W_{\text{SL}}} \right) \exp(-j2\pi f_\varphi t) \end{aligned} \quad (21)$$

For better comparison with other imaging modes, we define the following normalized version of the autocorrelation function

$$\begin{aligned} \bar{R}_{ii}(t, \tau) &= \frac{R_{ii}(t, \tau)}{R_{s_1 s_1}(0)R_{s_2 s_2}(0)} = \text{tri}^2 \left(\frac{k_a t}{W_{\text{SL}}} \right) \text{sinc}^2 [(W_{\text{SL}} - |k_a t|) t] \\ &\quad + \gamma_T^2 \text{tri}^2 \left(\frac{f_\varphi}{W_{\text{SL}}} \right) \exp(-j2\pi f_\varphi t) \end{aligned} \quad (22)$$

Then the normalized power spectral density of the spotlight SAR interferogram can be obtained by performing Fourier transform of (22)

$$\bar{S}_{ii}(f) = \frac{1}{W_{\text{SL}}} \text{tri} \left(\frac{f}{W_{\text{SL}}} \right) + \left| \gamma_T \text{tri} \left(\frac{f_\varphi}{W_{\text{SL}}} \right) \right|^2 \delta(f + f_\varphi) \quad (23)$$

Therefore, the normalized power spectral density of the strip-map SAR interferogram can also be obtained by the same method, which is given by

$$\bar{S}_{ii,\text{strip}}(f) = \frac{1}{W_{\text{strip}}} \text{tri} \left(\frac{f}{W_{\text{strip}}} \right) + \left| \gamma_T \text{tri} \left(\frac{f_\varphi}{W_{\text{strip}}} \right) \right|^2 \delta(f + f_\varphi) \quad (24)$$

where W_{strip} is the azimuth bandwidth of strip-map SAR.

From (23) and (24) we get that the power spectral density of the spotlight SAR interferogram is similar with the strip-map SAR. The difference between them is that their power spectral density distributions are limited by their own azimuth bandwidth. Consequently, the spotlight SAR interferometry can be processed with the similar method for strip-map SAR, but special steps should be considered to adapt the change of the bandwidth.

4. SPACEBORNE SPOTLIGHT SAR INTERFEROMETRY

The processing of spotlight SAR interferometry is almost the same as strip-map SAR. The great difference is that the space-variant spectrum of spotlight SAR must be taken into account when dealing with interferometric applications. The coregistration algorithm proposed in this paper contains coarse coregistration, azimuth spectral filter, and accurate coregistration. The detailed steps are listed in the following.

4.1. Coarse Coregistration

The slave image is resampled to the geometry of the master image based on the annotated information of the TerraSAR-X products first, then the spotlight SAR images are coarsely coregistered by the cross correlation of the detected amplitude images [18].

4.2. Azimuth Spectral Filter

The Doppler centroid values $f_{dc,1}$ and $f_{dc,2}$ of both spotlight images can be extracted from the annotated information of the TerraSAR-X products. If $f_{dc,1}$ is different from $f_{dc,2}$, the azimuth spectral filter is needed to extract the overlapping spectral part that can be processed to an interferogram. Based on the analysis of Section 2.2, the Doppler centroid frequency in the focused image of spotlight SAR varies near linearly with azimuth, and the Doppler rate is k_a , which looks as if a gross quadratic phase was superimposed on the spotlight SAR image. If we compensate that quadratic phase, the spectrum will become

azimuth-invariant. From (10), we can get that the function used for compensating the quadratic phase can be written as

$$h(\tau) = \exp(-j\pi k_a \tau^2) \quad (25)$$

As a first step, we multiply (10) by (25), resulting in

$$\begin{aligned} & \text{sinc}[W_{\text{SL}}(\tau - \tau_0)] \exp[j2\pi k_a \tau_0(\tau - \tau_0)] \exp(-j\pi k_a \tau^2) \\ &= \text{sinc}[W_{\text{SL}}(\tau - \tau_0)] \exp[-j\pi k_a(\tau - \tau_0)^2] \exp(-j\pi k_a \tau_0^2) \end{aligned} \quad (26)$$

Now the spectrum of each scene is of band-pass type. Consequently the common frequency band can be chosen using an azimuth bandpass filter.

$$h(f) = \begin{cases} 1 & \max(f_{dc,1} - W_1/2, f_{dc,2} - W_2/2) < f \\ & < \min(f_{dc,1} + W_1/2, f_{dc,2} + W_2/2) \\ 0 & \text{elsewhere} \end{cases} \quad (27)$$

where W_1 and W_2 are the bandwidths of the master image and the slave image, respectively. Finally, we compensate the gross quadratic phase by a multiplication with the conjugation of $h(\tau)$.

4.3. Coregistration with Adaptive Subspace Projection

The coregistered complex SAR images, denoted as $\mathbf{s}(i)$, of a pixel pair i (corresponding to the same ground area) can be modeled as [19]

$$\mathbf{s}(i) = \mathbf{a}(\varphi_i) \odot \mathbf{x}(i) + \mathbf{n}(i) \quad (28)$$

where $\mathbf{a}(\varphi_i) = [1, e^{j\varphi_i}]^T$ is array steering vector, while $\mathbf{x}(i)$ is the complex magnitude vector, and $\mathbf{n}(i)$ is the additive noise term. Define the joint data vector $\mathbf{S}(i)$ of pixel pair i as [20]

$$\mathbf{S}(i) = [\mathbf{s}(i-4)^T, \mathbf{s}(i-3)^T, \dots, \mathbf{s}(i+3)^T, \mathbf{s}(i+4)^T]^T \quad (29)$$

In order to simplify the computation, we suppose that the neighboring pixels have an identical terrain height, and then the joint covariance matrix can be written as

$$\mathbf{C}_S(i) = E\{\mathbf{S}(i)\mathbf{S}^H(i)\} = \mathbf{A}(\varphi_i)\mathbf{A}^H(\varphi_i) \odot \mathbf{R}_S(i) + \sigma_n^2\mathbf{I} \quad (30)$$

where $\mathbf{A}(\varphi_i) = [\mathbf{a}^T(\varphi_i), \mathbf{a}^T(\varphi_i), \dots, \mathbf{a}^T(\varphi_i)]^T$ is the joint array steering vector, and $\mathbf{R}_S(i)$ is the joint correlation coefficient matrix.

By eigendecomposing $\mathbf{C}_S(i)$ we can obtain the principal eigenvector $[\alpha_1, \alpha_2, \dots, \alpha_M]$, the noise eigenvector $[\alpha_{M+1}, \alpha_{M+2}, \dots, \alpha_N]$, and the noise power σ_n^2 , where M is the number of the principal eigenvalues. Then we can get

$$\mathbf{R}_S(i) = \text{abs}(\mathbf{C}_S(i) - \sigma_n^2\mathbf{I}) \quad (31)$$

Since $\mathbf{R}_S(i)$ does not contain the noise components, $\mathbf{R}_S(i)$ can be eigendecomposed into

$$\mathbf{R}_S(i) = \sum_{m=1}^M \lambda'_m \beta_m \beta_m^H \tag{32}$$

From (30) and (32) we get that the signal subspace spanned by $[\alpha_1, \alpha_2, \dots, \alpha_M]$ can also be spanned by $[\mathbf{A}(\varphi_i) \odot \beta_1, \mathbf{A}(\varphi_i) \odot \beta_2, \dots, \mathbf{A}(\varphi_i) \odot \beta_M]$.

Therefore, the interferometric phase φ_i can be estimated by projecting the joint signal subspace onto the joint noise subspace.

$$\varphi_i = \min \left\{ \sum_{m=1}^M \sum_{n=1}^{N-M} (\mathbf{A}(\varphi_i) \odot \beta_m)^H \alpha_{n+M} \alpha_{n+M}^H (\mathbf{A}(\varphi_i) \odot \beta_m) \right\} \tag{33}$$

Since in practice we are unable to obtain ensemble averages directly, the joint covariance matrix $\mathbf{C}_S(i)$ given by (30) is estimated by the corresponding sample covariance matrix of independent and identically distributed (i.i.d.) samples, which can be obtained from the neighboring pixels

$$\mathbf{C}_S(i) = \frac{1}{2(2K+1)} \sum_{k=-K}^K \mathbf{S}(i+k) \mathbf{S}^H(i+k) \tag{34}$$

where $2K+1$ denotes the number of i.i.d. samples, which is selected with a constant 35 in [20]. However, this method does not take into account the feature of the real spotlight SAR data.

According to the analysis of the subspace projection algorithm, we can find that the phase filtering contained in the method can be regarded as a slip window based filtering scheme, and the window size depends on the number of i.i.d. samples [21]. The interferogram noise will decrease with the increasing of the window size. However, the valid coherence information may also be impaired with an oversize window, and the estimation performance will decrease. Therefore, a suitable window size, equivalent to the number of i.i.d. samples used to estimate the joint covariance matrix, can be selected based on the signal-to-noise ratio, which can be reduced at areas with high signal-to-noise ratio and enlarged with low signal-to-noise ratio.

In addition, the signal-to-noise ratio can be related with the coherence value by [22]

$$\gamma = \frac{1}{1 + \text{SNR}^{-1}} \tag{35}$$

where γ denotes the coherence value, and SNR denotes the signal-to-noise ratio. From the relationship expressed in (35), the coherence can

be recognized as a direct measure of the interferogram noise. Therefore, it can be used to select the number of i.i.d. samples. Moreover, the coherence value can be estimated simply from the two complex SAR images s_1 and s_2 (the interferometric pair) [23]

$$\gamma = \frac{\left| \sum_{i=1}^N s_{1,i} s_{2,i}^* \right|}{\sqrt{\sum_{i=1}^N s_{1,i} s_{1,i}^* \sum_{m,n=0}^N s_{2,i} s_{2,i}^*}} \quad (36)$$

where subscript i denotes the i th pixel of N neighboring pixels averaged. Note that the coherence value is obtained approximating ensemble averages with spatial means here.

Consequently, an adaptive scale factor is introduced to select the number of i.i.d. samples based on the coherence value in this paper. Normally the coherence value larger than 0.7 has been considered as good coherence, so the number of i.i.d. samples corresponding to the coherence value 0.7 is selected to 35 as the initial sample number. Then, the required number of i.i.d. samples increases with the decreasing of the coherence value, and decreases with the increasing of the coherence value.

Thus, we assume that the expression of the number of i.i.d. samples used to estimate the joint covariance matrix can be written as

$$\text{Num} = \lceil \chi(\gamma) \times N_0 \rceil \quad (37)$$

where $\lceil \cdot \rceil$ rounds a number to the nearest integer, N_0 is the initial sample number, γ is the coherence value, and χ is the scale factor, which varies inversely with the coherence value

$$\chi(\gamma) = e^{0.7-\gamma} \quad (38)$$

Consequently, the required number of i.i.d. samples can be reduced at good coherence areas and enlarged at low coherence areas. Such a modification prevents the areas of high coherence (less noise) being overfiltered, but allows stronger filtering in areas where there is a low coherence (high noise).

Moreover, the forward/backward smoothing scheme is adopted for the joint covariance matrix to achieve superior performance [24]

$$\mathbf{C}_S(i) = \frac{1}{2(2K+1)} \left[\sum_{k=-K}^K \mathbf{S}(i+k) \mathbf{S}^H(i+k) + \mathbf{J} \left(\sum_{k=-K}^K \mathbf{S}(i+k) \mathbf{S}^H(i+k) \right) \mathbf{J} \right] \quad (39)$$

where \mathbf{J} is the inverse diagonal matrix, $2K + 1$ denotes the number of i.i.d. samples, and its value varying with the coherence value is obtained from (37).

4.4. Phase Unwrapping

The phases estimated from interferogram are still ambiguous by integer multiples of 2π . For applications such as terrain reconstruction from across-track interferograms, we must resolve this ambiguity. The Flynn's minimum discontinuity algorithm is a classic phase unwrapping method [25], which is guaranteed to produce a "minimum discontinuity" solution. Therefore, the Flynn's minimum discontinuity algorithm is selected to perform phase unwrapping in this paper.

Moreover, it seems that the flattening algorithms must be adopted to reduce the density of the interferogram before the phase estimation, which can make phase unwrapping easier [26].

5. PERFORMANCE INVESTIGATION

In this section, real spotlight SAR data obtained from TerraSAR-X on February 12 and 23, 2009 over the Ayers Rock region of Australia are used to perform interferometric processing.

Figure 2(a) shows the interferogram obtained by the conventional subspace projection method, and Figure 2(b) is the one obtained by the adaptive subspace projection method proposed in this paper. Comparing Figure 2(a) with Figure 2(b), it is observed that the

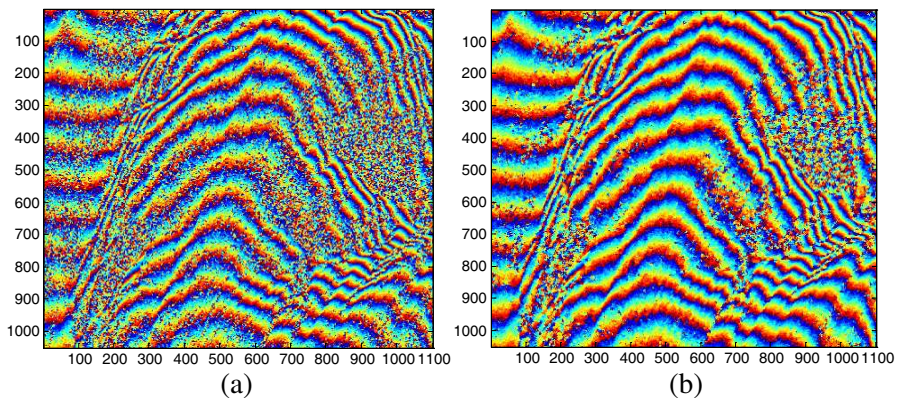


Figure 2. Interferogram obtained by (a) the subspace projection method, (b) the proposed method.

interferogram obtained by the proposed method is clearer than the subspace projection method. According to the analysis of the coherence histogram obtained by the coarse coregistration images, we find that the coherence values are lower at some areas (see Figure 3). If we use the uniform number of the samples to estimate the joint covariance matrix as it made by Li et al. [20], the result is not satisfactory. Therefore, the number of the samples used to estimate the joint covariance matrix is changeable and adaptive to the coherence

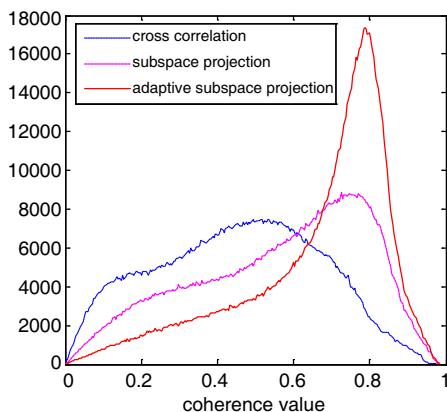


Figure 3. Coherence histograms of the three methods.

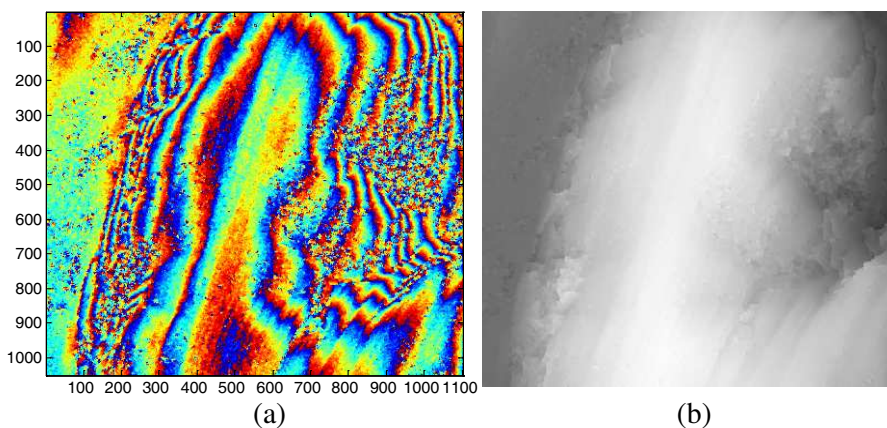


Figure 4. Interferogram and final unwrapped result. (a) Interferogram with flat-earth removed. (b) The unwrapped result using Flynn's minimum discontinuity algorithm.

value in the proposed method, and the result confirms the effectiveness of the proposed method in spotlight SAR interferometry.

The interferogram with flat-earth removed is given in Figure 4(a). Figure 4(b) shows the unwrapped result using Flynn's minimum discontinuity algorithm. It is observed that the algorithm can guarantee an unwrapped solution.

6. CONCLUSIONS

Spotlight SAR interferometry combines the advantage of high resolution spotlight mode and interferometry to obtain better detail information of interested scene. Therefore, this interferometric mode has great potential in the future. This paper gives an overview of the interferometric properties of spotlight SAR signals and analyzes the effect of the azimuth-variant Doppler to the interferometric processing. Moreover, a new coregistration method is proposed and the processing flow is given for spotlight SAR interferometry. The results of real data confirm the efficiency.

ACKNOWLEDGMENT

This work was supported by the Key Laboratory of Ministry of Education, College of Information Science and Engineering, Henan University of Technology. Moreover, the authors wish to thank DLR for providing the access to the spotlight SAR data used in this study.

REFERENCES

1. Chan, Y. K. and V. C. Koo, "An introduction to synthetic aperture radar (SAR)," *Progress In Electromagnetics Research B*, Vol. 2, 27–60, 2008.
2. Carrara, W. G., R. S. Goodman, and R. M. Majewski, *Spotlight Synthesis Aperture Radar Signal Processing Algorithms*, Artech House, Boston, London, 1995.
3. Guo, D., H. Xu, and J. Li, "Extended wavenumber domain algorithm for highly squinted sliding spotlight SAR data processing," *Progress In Electromagnetics Research*, Vol. 114, 17–32, 2011.
4. Mao, X., D.-Y. Zhu, and Z.-D. Zhu, "Signatures of moving target in polar format spotlight SAR image," *Progress In Electromagnetics Research*, Vol. 92, 47–64, 2009.

5. Rodriguez, E. and J. M. Martin, "Theory and design of interferometric synthetic aperture radars," *IEEE Proceedings — F*, Vol. 139, No. 2, 147–159, 1992.
6. Eineder, M., N. Adam, and R. Bamler, "Spaceborne spotlight SAR interferometry with TerraSAR-X," *IEEE Transactions on Geoscience and Remote Sensing*, Vol. 47, No. 5, 1524–1535, 2009.
7. Wu, B.-I., M. C. Yeung, Y. Hara, and J. A. Kong, "Insar height inversion by using 3-D phase projection with multiple baselines," *Progress In Electromagnetics Research*, Vol. 91, 173–193, 2009.
8. Li, C. and D.-Y. Zhu, "A residue-pairing algorithm for insar phase unwrapping," *Progress In Electromagnetics Research*, Vol. 95, 341–354, 2009.
9. Li, S., H. Xu, and L. Zhang, "An advance DSS-SAR insar terrain height estimation approach based on baseline decoupling," *Progress In Electromagnetics Research*, Vol. 119, 207–224, 2011.
10. Adam, N., M. Eineder, N. Yague-Martinez, and R. Bamler, "TerraSAR-X high resolution SAR-interferometry," *7th European Conference on Synthetic Aperture Radar*, 2008.
11. Gernhardt, S. and R. Bamler, "Towards deformation monitoring of single buildings — persistent scatterer interferometry using TerraSAR-X very high resolution spotlight data," *8th European Conference on Synthetic Aperture Radar*, 2010.
12. Adam, N., X. X. Zhu, C. Minet, W. Liebhart, M. Eineder, and R. Bamler, "Techniques and examples for the 3D reconstruction of complex scattering situations using TerraSAR-X," *IEEE International Geoscience and Remote Sensing Symposium*, Vol. 3, 990–903, 2009.
13. Even, M., A. Schunert, K. Schulz, and U. Soergel, "Atmospheric phase screen-estimation for PSInSAR applied to TerraSAR-X high resolution spotlight-data," *IEEE International Geoscience and Remote Sensing Symposium*, 2928–2931, 2010.
14. Baade, J. and C. C. Schmullius, "Interferometric microrelief sensing with TerraSAR-X — first results," *IEEE Transactions on Geoscience and Remote Sensing*, Vol. 48, No. 2, 965–970, 2010.
15. Zebker, H. A. and J. Villasenor, "Decorrelation in interferometric radar echoes," *IEEE Transactions on Geoscience and Remote Sensing*, Vol. 30, 950–959, 1992.
16. Breit, H., T. Fritz, U. Bals, M. Lachaise, A. Niedermeier, and M. Vonavka, "TerraSAR-X SAR processing and products," *IEEE Transactions on Geoscience and Remote Sensing*, Vol. 48, No. 2, 727–740, 2010.

17. Holzner, J. and R. Bamler, "Burst-mode and ScanSAR interferometry," *IEEE Transactions on Geoscience and Remote Sensing*, Vol. 40, No. 9, 1917–1934, 2002.
18. Lin, Q., J. F. Vesecky, and H. A. Zebker, "New approaches in interferometric SAR data processing," *IEEE Transactions on Geoscience and Remote Sensing*, Vol. 30, No. 3, 560–567, 1992.
19. Ren, X.-Z., L. H. Qiao, and Y. Qin, "A three-dimensional imaging algorithm for tomography SAR based on improved interpolated array transform," *Progress In Electromagnetics Research*, Vol. 120, 181–193, 2011.
20. Li, Z., Z. Bao, H. Li, and G. Liao, "Image autocoregistration and InSAR interferogram estimation using joint subspace projection," *IEEE Transactions on Geoscience and Remote Sensing*, Vol. 44, No. 2, 288–297, 2006.
21. Eichel, P. H., D. C. Ghiglia, C. V. Jakowatz, P. A. Thompson, and D. E. Wahl, "Spotlight SAR interferometry for terrain elevation mapping and interferometric change detection," *Sandia National Laboratories, Technique Report SAND*, 1993.
22. Bamler, R. and D. Just, "Phase statistics and decorrelation in SAR interferograms," *IEEE Geoscience and Remote Sensing Symposium*, Vol. 3, 980–984, 1993.
23. Zebker, H. A. and K. Chen, "Accurate estimation of correlation in InSAR observations," *IEEE Geoscience and Remote Sensing Letters*, Vol. 2, No. 2, 124–127, 2005.
24. Delis, A. and G. Papadopoulos, "Enhanced forward/backward spatial filtering method for DOA estimation of narrowband coherent sources," *IEE Proceedings — Radar, Sonar and Navigation*, Vol. 43, No. 1, 10–16, 1996.
25. Flynn, T. J., "Two-dimensional phase unwrapping with minimum weighted discontinuity," *Journal of the Optical Society of America A*, Vol. 14, No. 10, 2692–2701, 1997.
26. Xiang, Z., K. Z. Wang, and X. Z. Liu, "A new DEM reconstruction method based on accurate flattening algorithm in interferometric SAR," *International Conference on Acoustics, Speech, and Signal Processing*, 1093–1096, 2008.